The $^{9}Be(p,p_0)^{9}Be$, $^{9}Be(p,d_0)^{8}Be$, and $^{9}Be(p,\alpha_0)^{6}Li$ cross-sections for analytical purposes

S. Krat[a,b], M. Mayer[b], C. Porosnicu[c]

[a]*National Research Nuclear University MEPhI (Moscow Engineering Physics Institute), Moscow Kashirskoe road 31, 115409, Russia*

[b]*Max-Planck-Institut für Plasmaphysik, Boltzmannstr. 2, 85748 Garching, Germany*

[c]*National Institute for Laser, Plasma and Radiation Physics, Atomistilor 409, Magurele, Jud Ilfov, 077125, Bucharest, Romania*

Abstract

The cross-sections for the $^{9}Be(p,d_0)^{8}Be$ nuclear reaction and for $^{9}Be(p,p_0)^{9}Be$ backscattering were measured at a laboratory scattering angle of 165° in the energy range from 400 to 4150 keV, the cross-section for the $^{9}Be(p,\alpha_0)^{6}Li$ nuclear reaction was determined in the energy range from 400 to 1300 keV. The cross-sections were determined using thin films. The absolute accuracies are about 4.4 – 8.6% for the backscattering, 4.6 – 24% for the $^{9}Be(p,d_0)^{8}Be$ nuclear reaction, and 4.5 – 5% for the $^{9}Be(p,\alpha_0)^{6}Li$ nuclear reaction cross-section. The derived cross-section data were benchmarked in the energy range 1100 – 4100 keV by comparison to measured spectra from bulk beryllium. The cross-section data are presented in graphical and tabular forms.

Keywords

Cross-section; Beryllium; Proton; Ion beam analysis; Backscattering analysis; Nuclear reaction analysis

Introduction

Beryllium is an important material for use in plasma-facing components of controlled fusion devices due to its low nuclear charge, relatively high melting point, and its ability to getter oxygen. In 2010 the first wall of the JET tokamak has been changed from carbon to beryllium and tungsten [1], with first results showing significant improvements with respect to wall erosion and hydrogen isotopes retention [2-5]. Beryllium is also planned to be used in plasma-facing components of the ITER tokamak, which is currently being built in Cadarache, France. Due to its low mass density and high elastic modulus beryllium is also being used as lightweight construction material, for example in aerospace applications. Beryllium appears naturally in some minerals (for example Beryll) and is used in some alloys, for example CuBe or CuCoBe.

Elastic backscattering spectrometry (EBS) is a versatile method for the quantitative analysis of the near-surface composition of solids. In fusion research it is often used for quantitative measurements of material erosion and deposition processes by analyzing wall samples from fusion devices [5-9]. Using EBS with incident protons makes it possible to analyze even very thick surface layers: For light elements such as Be or C layer thicknesses up to about 50 µm can be analyzed. For the analysis of thick layers large backscattering angles in the range 160° - 170° are advantageous. However, EBS requires accurate knowledge of the cross-section data to produce accurate results. The backscattering cross-section of protons from beryllium is Rutherford only at very low energies below about 230 keV [10]. At higher energies the cross-section is enhanced compared to the Rutherford cross-section. Unfortunately there are only scarce data available for the $^{9}Be(p,p_0)^{9}Be$ backscattering cross-section, which are at least twenty years old [10-14]. Three data sets are close to a scattering angle of 160° [11, 13-14], but each covers only a limited energy range. The data by Liu [10] cover the whole energy range from 0.15 to 3 MeV at a scattering angle of 170°. At energies above 3 MeV data get very scarce, and here is a gap in the data between 3.79 and 4 MeV. For scattering angles between 161° and 170° no data are available. Sufficiently accurate theoretical data, for example from SigmaCalc, are also not available.

In addition to backscattering, there are several nuclear reactions of protons with ^{9}Be:

$^{9}Be+p \rightarrow d_0+^{8}Be$ (I)

$^{9}Be+p \rightarrow \alpha_0+^{6}Li$ (II)

$^{9}Be+p \rightarrow \alpha_1+^{6}Li$ (III)

Reaction (I) has a relatively large cross-section in the energy range 1-2.5 MeV and has to be taken into account when analyzing thick Be layers. The lifetime of the produced ^{8}Be is very short and it further disintegrates into two α-particles. Cross-section data for these reactions are only available either at low energies below 900 keV [15], or for detector angles below about 138° [16-17]. The cross-section data are at least 40 years old.

Data for reactions (II) and (III) are very scarce [15-16]. The data by Bertrand et al. [15] are close to a reaction angle of 160° and cover the energy range 0.3 to 0.9 MeV. However, this data set contains only very few data points. The most comprehensive data set from Thomas et al. [16] was published already in the year 1949 and is for a reaction angle of 138°.

In this paper, cross-section data for $^{9}Be(p,p_0)^{9}Be$ backscattering and for the $^{9}Be(p,d_0)^{8}Be$ and $^{9}Be(p,\alpha_0)^{6}Li$ nuclear reactions are presented at an angle of 165°.

Experimental

The measurements were performed using a beryllium-compatible glove box at the 3 MV tandem accelerator of the Max-Planck-Institut für Plasmaphysik in Garching. The accuracy of the incident beam energy is about ±10 keV. This was determined by using the $^{27}Al(p,\gamma)^{28}Si$ reaction at 992 keV, by matching peak positions from an Al EBS spectrum modeled using the SigmaCalc cross-section [18] at 1598 keV and by matching peak positions from an Al EBS

spectrum modeled using the cross-section from [19] at 2890 keV. The incident beam energy spread is below 1 keV. The backscattering spectrum and nuclear reaction products were recorded using a detector with a solid angle of 1.72×10^{-3} sr located at a scattering angle of 165°. The scattering angle is known with an accuracy better than $\pm1°$, and the error of the solid angle is 1.5%. The solid angle was determined by measuring four GEEL calibration samples: (22.4 ± 0.4) μg/cm² Au on Si, $(48.1\pm0.6)\times10^{15}$ at/cm² Sb implanted in Si/SiO_2, (34.0 ± 2.4) μg/cm² Pd on vitreous carbon and (22.0 ± 0.6) μg/cm² Ti on vitreous carbon, and averaging the results. The uncertainty of the solid angle was calculated as the scatter of multiple measurements.

Three samples were used to measure the cross-sections in different energy ranges. The samples consisted of polished pyrolytic graphite with a sputter-deposited Al layer on top: 3.3×10^{18} at/cm², 27×10^{18} at/cm² and 58×10^{18} at/cm², respectively. On top of the aluminum a thin Au layer with a thickness of 7.7×10^{16} at/cm² was evaporated, and on top of the gold a Be layer with a thickness of 4.4×10^{18} at/cm² was deposited using a thermionic vacuum arc [20]. The thicknesses of the Al layers were checked with EBS prior to the Au evaporation using the SIMNRA code [21] with SRIM 2013 stopping powers [22] and backscattering cross-section data from [19]. The purpose of the Al layers was to shift the signal of the C substrate towards lower energies in order to separate it from the Be signal, so that the Be signal could be measured more precisely with smaller background contribution from the substrate.

The samples for the cross-section measurements were analyzed with proton energies from 400 to 4150 keV with a 50 keV step and 5 μC of charge per measurement.

In addition, bulk Be and Au samples were measured as benchmark with energies from 1.1 to 3.7 MeV with a 200 keV step and 5 μC of charge per measurement. The bulk Be sample was clean enough that no distinctive peaks of other elements than oxygen were observed in the EBS spectra. The detected amount of O on the Be bulk sample was about 4×10^{16} at/cm².

Experimental results

3.1. Be/Au/Al/C multilayers

Typical spectra for bombardment of the multilayered samples 1, 2 and 3 with 2.2 MeV protons are shown in Fig. 1a, b and c respectively. The Au and Al peaks are well separated from the C background and from each other. The $^{9}Be(p,d_0)^{8}Be$ reaction peak and the $^{9}Be(p,p_0)^{9}Be$ backscattering peak can also be easily distinguished from each other. In Fig. 1a the $^{9}Be(p,d_0)^{8}Be$ reaction peak and the $^{9}Be(p,p_0)^{9}Be$ backscattering peak overlap with the signal from the carbon substrate, and in Fig. 1c they overlap with the Al peak. In Fig. 1b both Be peaks are located between the C and Al signals with only little background, resulting in a decreased statistical error for the peak integrals. Depending on incident beam energy this required varying Al layer thicknesses. Incident proton energy ranges and the corresponding sample numbers in which a low background similar to Fig. 1b could be achieved are shown in table 1. Within energy ranges not listed in table 1 overlap with the signal from the carbon substrate could not be avoided, resulting in larger statistical uncertainties. It should be also noted that for energies from 2.45 to 2.95 MeV the energies of backscattered protons and of deuterons from the $^{9}Be(p,d_0)^{8}Be$ reaction

overlap and can't be distinguished (Fig 2). In that energy range, only the sum of the cross-sections was obtained. Alpha particles originating from the ^{9}Be(p,α_0)^{6}Li reaction could be reliably separated from background or other peaks only at energies below 1.3 MeV. A typical spectrum for bombardment of the multilayered sample 1 with 1.3 MeV protons is shown in Fig 3 – a low, wide ^{9}Be(p,α_0)^{6}Li nuclear reaction peak can be seen at energies above the Au backscattering peak. Alpha particles originating from the ^{9}Be(p,α_1)^{6}Li reaction couldn't be reliably discerned from background at any energy.

The differential cross-sections $\sigma_{^9Be}$, σ_{d_0} and σ_{α_0} the backscattering from ^{9}Be, for the ^{9}Be(p,d_0)^{8}Be reaction and for the ^{9}Be(p,α_0)^{6}Li reaction, respectively, are given by

$$\sigma_{^9Be} = \frac{N_{^9Be}}{N_{Au}} \frac{\rho_{Au}}{\rho_{Be}} \sigma_{Au} \qquad (1)$$

$$\sigma_{d_0} = \frac{N_{d_0}}{N_{Au}} \frac{\rho_{Au}}{\rho_{Be}} \sigma_{Au} \qquad (1)$$

$$\sigma_{\alpha_0} = \frac{N_{\alpha_0}}{N_{Au}} \frac{\rho_{Au}}{\rho_{Be}} \sigma_{Au} \qquad (1)$$

where $N_{^9Be}$ $N_{^9Be}$, N_{d_0} and N_{α_0} are the number of protons backscattered from ^{9}Be, the number of detected deuterons in the d0 peak and the number of detected alpha particles in the α_0 peak respectively, ρ_{Au}/ρ_{Be} ρ_{Au}/ρ_{Be} is the ratio of the areal densities of the gold and beryllium layers, N_{Au} N_{Au} is the number of protons backscattered from the Au layer, and σ_{Au} the cross-section for proton backscattering from gold. Eqs. (1), (2) and (3) use only count ratios measured within the same spectrum, and uncertainties of the solid angle and of beam charge integration cancel out in eqs. (1), (2) and (3). The cross-section for backscattering from gold is Rutherford at energies below about 9 MeV. One can therefore use

$$\sigma_{Au} = f \sigma_{Au}^{R} \qquad (1)$$

where σ_{Au}^{R} is the Rutherford cross-section for proton backscattering and f is a small correction factor close to unity due to electron shielding of the Au nuclear charge. Andersen screening [23] was used to calculate the screened cross-section. The deviation of f from unity is below 0.5% for incident proton energies above 1.7 MeV.

The energy losses of protons in the Au and Be layers were calculated using SRIM-2013 stopping power data. The energy losses in the Au layer are smaller than 5.8 keV and smaller than 23 keV for the Be layers. The largest energy losses occur at the lowest energies and get smaller with increasing energy. These energy losses were taken into account in the calculation of the mean energy in each layer. To account for changes in the cross-sections within the layers, mean energies were used according to

$$\overline{E}_{Be} = E_0 - \frac{\Delta E_{Be}}{2} \qquad (1)$$

$$\overline{E}_{Au} = E_0 - \Delta E_{Be} - \frac{\Delta E_{Au}}{2} \qquad (1)$$

where E_0 is the incident proton energy, $\overline{E}_{Be}$ and $\overline{E}_{Au}$ the mean energies in the Be and Au layers respectively, and ΔE_{Be} and ΔE_{Au} the energy losses in the Be and Au layers, respectively.

By using the ratio to the Rutherford cross-section from gold according to eq. (2) the relative shape of the cross-section as function of energy can be determined. For absolute cross-section values the ratio of the areal densities of Au and Be must be known. This ratio can be determined by using either protons at sufficiently low energies, so that the scattering cross-sections from Au and Be are both Rutherford, or by using incident ^{4}He ions at sufficiently low energies [24]. Backscattering of protons from Be gets Rutherford at energies below about 300 keV [10], and below about 1300 keV for ^{4}He [25]. Unfortunately it was not possible to measure at these low energies due to the thickness of the Be layer. Because of this, data obtained from a bulk beryllium sample were used for absolute calibration. Using the bulk beryllium sample at 2.1 MeV incident proton energy, the cross-sections for the ^{9}Be(p,d$_0$)^{8}Be reaction and ^{9}Be(p,p$_0$)^{9}Be backscattering were scaled to provide the best possible fit (Fig. 4). The alpha particle signal of the ^{8}Be→2×^{4}He fission reaction and the ^{9}Be+p→α$_0$+6Li reaction was extrapolated (Fig. 4, dashed line) and subtracted from the data. This absolute calibration relies on the SRIM 2013 stopping power for protons in beryllium, which is accurate within about 4% [22]. Moreover, this absolute calibration needs to use the measured values for detector solid angle times integrated beam charge, which increases the total uncertainty to 4.3%. In order to check the accuracy of the measurement of detector solid angle times integrated beam charge a bulk gold sample was measured as well and simulated using the screened Rutherford cross-section (eq. 4) and SRIM-2013 stopping powers. The simulated spectrum agreed with the measured spectrum within about 4%, i.e. within the uncertainty of the SRIM stopping power. This shows that our normalization procedure is correct within the given uncertainties.

3.2. The ^{9}Be(p,p$_0$)^{9}Be backscattering cross-section

The ^{9}Be(p,p$_0$)^{9}Be backscattering cross-section was determined using eq. (1) and absolutely quantified by using the bulk Be spectrum (see section 3.1 and Fig. 4). The differential cross-section in the laboratory system is shown in fig. 5 together with the data from Liu [10], Allab [11], Yasue [12], Mashkarov [13], and Tsan [14]. The determined cross-section values are tabulated in table 2. The proton energy in this table is the mean energy in the beryllium layer. For the energy range of incident protons from 2450 keV to 2950 keV protons backscattered from 9Be and deuterons from the ^{9}Be(p,d$_0$)^{8}Be nuclear reaction overlap. Because in general the ^{9}Be(p,p$_0$)^{9}Be cross-section is much higher than the ^{9}Be(p,d$_0$)^{8}Be cross-section, the cross-section for the sum of reactions obtained in this range was assumed to be cross-section of ^{9}Be(p,p$_0$)^{8}Be. However, it should be kept in mind that cross-section data from the energy range 2450-2950 keV should be used with some care.

The error bars take into account the statistical error for the p_0 and Au peak integrals ranging from 1.2% to 7.5% with an average error of 3%, the uncertainty of the solid angle for the bulk beryllium measurements (1.5%), and the uncertainty of the SRIM 2013 stopping power used to quantify the cross-section (4.0%). Where possible, data from two samples were used to calculate the average cross-section for a given energy, decreasing the statistical error. The total uncertainty is between 4.4 and 8.6%, with an average uncertainty of 5.4%. The shape of the cross-section curve and the absolute values of the cross-section are in good agreement with Liu's data for 170°, as well as with Allab's data for 158.3°, Tsan's data for 158.7° and Yasue's data for 150°. The maximum close to 2.5 MeV is smaller in Mashkarov's data at 160.9°, while our data are in good agreement with Liu. The position of the peak is the same in our work, Mashkarov and Liu.

3.3. The $^{9}Be(p,d_0)^{8}Be$ nuclear reaction cross-section

The relative shape of the $^{9}Be(p,d_0)^{8}Be$ nuclear reaction cross-section was determined from eq. (2) and absolutely quantified by using the bulk Be spectrum (see section 3.1 and Fig 4). The differential cross-section in the laboratory system is shown in fig. 6 together with the data from Bertrand [15], Thomas [16], and Weber [17]. The cross-section values are tabulated in table 3. The incident protons lose between 4.6 and 22.7 keV in the Be layer for incident energies between 400 and 4150 keV. The proton energy in table 2 is the mean energy in the beryllium layer.

The deuterons from the $^{9}Be(p,d_0)^{8}Be$ nuclear reaction overlap with protons backscattered from 9Be for incident proton energies from 2450 to 2950 keV, see Fig. 2. Within this energy range the $^{9}Be(p,d_0)^{8}Be$ nuclear reaction cross-section therefore cannot be determined.

The error bars take into account the statistical error for the number of counts in the d_0 and Au peaks ranging from 1.7% to 23% with an average error of 11%, the uncertainty for the product of solid angle times integrated beam charge for the bulk beryllium measurement used for absolute quantification of the cross-section (1.5%), and the uncertainty of the SRIM 2013 stopping power [22] (4.0%). Where possible, data from two samples were used to calculate the average cross-section for a given energy, decreasing the statistical error. The resulting total uncertainty for the cross-section is between 4.6% and 24% with an average uncertainty of about 12%. The highest uncertainties are in the range of incident energies from 3 to 4.15 MeV.

At energies below about 1.3 MeV our data are in good agreement with Bertrand, who measured at a comparable angle, but also with Thomas and Weber despite the fact that they measured at reaction angles of 135-138°. At energies above about 1.3 MeV the shape of the cross-section curve is in general agreement with Weber's data, indicating maxima at roughly the same energies. However, the absolute values differ from Weber's data by up to a factor of 2. It should be noted that there is already a discrepancy between Weber's and Thomas' data at the highest energies, with good agreement of our data with Thomas but disagreement with Weber. The detection angle in this work (165°) differs considerably from the angles used by Thomas (138°) and Weber (135°), which might account for the difference in absolute values. But it cannot be excluded that Weber's data have a large systematic error above 1.3 MeV.

3.4. The $^{9}Be(p,\alpha_0)^{6}Li$ nuclear reaction cross-section

The relative shape of the $^{9}Be(p,\alpha_0)^{6}Li$ nuclear reaction cross-section was determined from eq. (3) and absolutely quantified by using the bulk Be spectrum (see section 3.1 and Fig 4). The differential cross-section in the laboratory system is shown in fig. 7 together with the data from Bertrand [15] and Thomas [16]. The determined cross-section values are tabulated in table 4. The proton energy in this table is the mean energy in the beryllium layer.

At energies ranging from about 0.8 MeV to about 1.2 MeV our data are in good agreement with Bertrand, who measured at a comparable angle, but also with Thomas despite the fact that they measured at a reaction angle of 138°. At energies above about 1.2 MeV our data are higher than Thomas data by about 30%. This discrepancy might be caused by the different reaction angles or by larger uncertainties in Thomas' data.

The α_0 peak appears at energies above the incident beam energy (see Figs. 2 and 3) and is therefore almost background-free, resulting in small statistical uncertainties. The error bars take into account the statistical error for the α_0 and Au peaks ranging from 1.5% to 2.7% with an average error of 1.8%, the uncertainty of the solid angle for the bulk beryllium measurements (1.5%), and the uncertainty of the SRIM 2013 stopping power used to quantify the cross-section (4.0%). Where possible, data from two samples was used to calculate the average cross-section for a given energy, decreasing the statistical error. The total uncertainty is between 4.5 and 5%, with an average uncertainty of 4.6%.

4. Benchmark measurements

The experimentally measured spectra of a polished bulk beryllium sample and the corresponding simulations using the measured cross-section data and SRIM-2013 stopping powers are shown in figure 8 a-n for incident proton energies of 1.1, 1.3, 1.5, 1.7, 1.9, 2.3, 2.5, 2.7, 2.9, 3.1, 3.3, 3.5, 3.7, 4.1 MeV. The simulations depend on the product of solid angle times ion fluence, which has been determined with an accuracy of 1.5%, and the accuracy of the stopping power of about 4%. The overall accuracy of the simulation is therefore about 4.3%. The accuracy of the benchmark measurements has been checked with a bulk Au sample at energies of 1.1, 1.3, 1.5, 1.7, 1.9, 2.3, 2.5, 2.7, 2.9, 3.1, 3.3, 3.5, 3.7, 4.1 MeV. The simulations for the bulk Au sample agreed within 2 – 6% depending on energy with an average error of 4.2%, i.e. within the uncertainty of the stopping power.

The $^{9}Be(p,\alpha_i)^{6}Li$ nuclear reaction was included in simulations for 1.1 and 1.3 MeV incident proton energies. At higher energies cross-section data are not available.

The simulated spectra are in good agreement with the experimental spectra at most of the energies. The general shape of the spectra is the same, and the positions of resonance peaks seen at incident energies of 1.1, 2.7, 2.9, 3.1 MeV are identical for modeled and experimental spectra.

The lower simulated signals for 1.9 MeV incident proton energy is due to the alpha particle signal of the $^{8}Be \rightarrow 2\times^{4}He$ and the $^{9}Be(p,\alpha_i)^{6}Li$ reactions, which is not accounted for due to the lack of cross-section data at that energy.

Starting from 3.1 MeV incident energy the simulated spectra indicate small peaks where none are present in the experimental data. This is due to the scatter of the measured $^{9}Be(p,p_0)^{9}Be$ backscattering cross-section at incident energies above 3 MeV. The benchmark measurements indicate that the cross-section is relatively smooth at these energies, and the scatter of the cross-section values therefore seems to have no nuclear physics origin. Because modern day simulating software [21] doesn't take cross-section uncertainties into account, it cannot automatically compensate for such errors. To provide a practically usable cross-section for simulation purposes a smoothed version of $^{9}Be(p,p_0)^{9}Be$ backscattering cross-section was produced for incident energies range from 2.8 to 4.15 MeV. A Savitzky-Golay filter [26] was used to smooth the cross-section by 3rd order 10 point polynomials. The spectra obtained using this smoothed cross-section are shown in fig. 8i-n, and the smoothed cross-section values are shown in table 2.

Conclusions

The cross-sections for the $^{9}Be(p,d_0)^{8}Be$ nuclear reaction and for $^{9}Be(p,p_0)^{9}Be$ backscattering were measured at a laboratory scattering angle of 165° in the energy range from 400 to 4150 keV, the cross-section for the $^{9}Be(p,\alpha_0)^{6}Li$ nuclear reaction was determined in the energy range from 400 to 1300 keV. The absolute uncertainties are about 4.4 – 8.6% for the backscattering, 4.6 – 24% for the $^{9}Be(p,d_0)^{8}Be$ nuclear reaction, and 4.5 – 5% for the $^{9}Be(p,\alpha_0)^{6}Li$ nuclear reaction cross-section. The determined backscattering cross-section is in good agreement with available data for scattering angles in the range of 150° - 170° [10-14]. The determined $^{9}Be(p,d_0)^{8}Be$ nuclear reaction cross-section agrees with the data obtained by Bertrand, Thomas and Weber [15-17] at energies below about 1200 keV. At higher energies only data by Weber are available, where our data deviate by a factor of up to two. The angular dependence of the cross-section may account for this difference, but this may also indicate that Weber's data show a systematic error. The determined $^{9}Be(p,\alpha_0)^{6}Li$ nuclear reaction cross-section agrees with the data by Bertrand and Thomas at energies below about 1.2 MeV, but disagrees with Thomas' data at higher energies by about 30%. The determined cross-section data were benchmarked using a bulk beryllium sample in the energy range 1.1 – 4.1 MeV.

Acknowledgements

The technical assistance during all accelerator-based measurements by M. Fusseder and J. Dorner and ion-beam analysis measurements and data analysis by T. Hoffmann are gratefully acknowledged. The aluminum layers have been deposited by F. Koch, the gold layers were deposited by A. Manhard. The assistance of C. Lungu with deposition of the beryllium layers is acknowledged.

References

[1] G.F. Matthews, M. Beurskens, S. Brezinsek, M. Groth, E. Joffrin, A. Loving, M. Kear, M.L. Mayoral, R. Neu, P. Prior, V. Riccardo, F. Rimini, M. Rubel, G. Sips, E. Villedieu, P.d. Vries, M.L. Watkins, E.-J. contributors, JET ITER-like wall—overview and experimental programme, Physica Scripta, T145 (2011) 014001.

[2] A. Widdowson, E. Alves, C.F. Ayres, A. Baron-Wiechec, S. Brezinsek, N. Catarino, J.P. Coad, K. Heinola, J. Likonen, G.F. Matthews, M. Mayer, M. Rubel, J.-E. contributors, Material migration patterns and overview of first surface analysis of the JET ITER-Like Wall, PFMC-2013 conference, (2013).

[3] J.P. Coad, E. Alves, N.P. Barradas, A. Baron-Wiechec, N. Catarino, K. Heinola, J. Likonen, M. Mayer, G.F. Matthews, P. Petersson, A. Widdowson, J.-E. Contributors, Surface analysis of tiles and samples exposed to the first JET campaigns with the ITER-like wall, Physica Scripta, 2014 (2014) 014012.

[4] K. Heinola, C.F. Ayres, A. Baron-Wiechec, J.P. Coad, J. Likonen, G.F. Matthews, A. Widdowson, J.-E. Contributors, Tile profiling analysis of samples from the JET ITER-like wall and carbon wall, Physica Scripta, T159 (2014) 014013.

[5] S. Krat, Y. Gasparyan, A. Pisarev, I. Bykov, M. Mayer, G. de Saint Aubin, M. Balden, C.P. Lungu, A. Widdowson, Erosion at the inner wall of JET during the discharge campaign 2011–2012 in comparison with previous campaigns, Journal of Nuclear Materials, 456 (2015) 106-110.

[6] M. Mayer, R. Behrisch, K. Plamann, P. Andrew, J.P. Coad, A.T. Peacock, Wall erosion and material transport to the Mark I carbon divertor of JET, Journal of Nuclear Materials, 266–269 (1999) 604-610.

[7] S. Krat, J.P. Coad, Y. Gasparyan, A. Hakola, J. Likonen, M. Mayer, A. Pisarev, A. Widdowson, Erosion and deposition on JET divertor and limiter tiles during the experimental campaigns 2005–2009, Journal of Nuclear Materials, 438, Supplement (2013) S742-S745.

[8] M. Mayer, S. Krat, J.P. Coad, A. Hakola, J. Likonen, S. Lindig, A. Widdowson, Erosion at the inner wall of JET during the discharge campaigns 2001–2009, Journal of Nuclear Materials, 438, Supplement (2013) S780-S783.

[9] A. Baron-Wiechec, A. Widdowson, E. Alves, A.C. F, N.P. Barradas, S. Brezinsek, J.P. Coad, N. Catarino, K. Heinola, J. Likonen, G.F. Matthews, M. Mayer, P. Petersson, M. Rubel, W. van Renterghem, I. Uytdenhouwen, Global erosion and deposition patterns in JET with the ITER-like Wall, Journal of Nuclear Materials.

[10] Z. Liu, W. Rong, Non-Rutherford elastic scattering cross sections for 170° backscattering of 0.15-3.00 MeV protons from beryllium, Nuclear Inst. and Methods in Physics Research, B, 93 (1994) 404-408.

[11] M. Allab, A. Boucenna, M. Haddad, Excited States of **1**0B in the **9B plus p Elastic Scattering at 2 less than equivalent to E//p less than equivalent to 5 Mev, Journal de physique Paris, 44 (1983) 579-588.

[12] M. Yasue, T. Ohsawa, N. Fujiwara, S. Kakigi, D.C. Nguyen, S. Yamashita, Excited states of 10B near 10 MeV studied by proton induced reactions on 9Be, Journal of the Physical Society of Japan, 33 (1972) 265.

[13] Ju.G.Mashkarov, A.S.Dejneko, R.P.Slabospickij, I.I.Zaljubovskij, R-matrix theory analysis of the polarized protons elastic scattering on the 9Be nuclei, Izvestiya Rossiiskoi Akademii Nauk, Ser. Phys., 40 (1976).

[14] M. Tsan, W.F. Hornyak, B10 levels from elastic scattering of protons by Be9, Physical Review, 187 (1969) 1220-1233.

[15] F. Bertrand, G.Grenier, J.Pornet, Study of the reactions 9Be(p,a)6Li,9Be(p,d)8Be from 300 keV to 900 keV, in: Saclay Reports, Centre d`Etudes Nucleaires, 1968.

[16] R.G. Thomas, S. Rubin, W.A. Fowler, C.C. Lauritsen, Beryllium-proton reactions and scattering [11], Physical Review, 75 (1949) 1612-1613.

[17] G. Weber, L.W. Davis, J.B. Marion, (p,Â d) and (p,Â α) reactions in Be9, Physical Review, 104 (1956) 1307-1313.

[18] D. Abriola, N.P. Barradas, I. Bogdanović-Radović, M. Chiari, A.F. Gurbich, C. Jeynes, M. Kokkoris, M. Mayer, A.R. Ramos, L. Shi, I. Vickridge, Development of a reference database for Ion Beam Analysis and

future perspectives, Nuclear Instruments and Methods in Physics Research, Section B: Beam Interactions with Materials and Atoms, 269 (2011) 2972-2978.
[19] M. Chiari, L. Giuntini, P.A. Mandò, N. Taccetti, Proton elastic scattering cross-section on aluminum from 0.8 to 3 MeV, Nuclear Instruments and Methods in Physics Research, Section B: Beam Interactions with Materials and Atoms, 174 (2001) 259-266.
[20] C.P. Lungu, I. Mustata, V. Zaroschi, A.M. Lungu, A. Anghel, P. Chiru, M. Rubel, P. Coad, G.F. Matthews, Beryllium coatings on metals for marker tiles at JET: Development of process and characterization of layers, Physica Scripta T, T128 (2007) 157-161.
[21] M. Mayer, SIMNRA User's Guide, in, Max-Planck-Institut für Plasmaphysik, Germany, Garching, Germany, 1997.
[22] J.F. Ziegler, SRIM.org, in.
[23] H.H. Andersen, F. Besenbacher, P. Loftager, W. Möller, Large-angle scattering of light ions in the weakly screened Rutherford region, Physical Review A, 21 (1980) 1891-1901.
[24] M. Mayer, A. Annen, W. Jacob, S. Grigull, The 11B(p,α0)8Be nuclear reaction and 11B(p,p)11B backscattering cross sections for analytical purposes, Nuclear Instruments and Methods in Physics Research, Section B: Beam Interactions with Materials and Atoms, 143 (1998) 244-252.
[25] Z.S. Zheng, J.R. Liu, X.T. Cui, W.K. Chu, Cross sections for light element analysis by non-Rutherford scattering, Nuclear Instruments and Methods in Physics Research, Section B: Beam Interactions with Materials and Atoms, 118 (1996) 214-218.
[26] A. Savitzky, M.J.E. Golay, Smoothing and differentiation of data by simplified least squares procedures, Analytical Chemistry, 36 (1964) 1627-1639.

Table 1 – Incident proton energy ranges for the three samples in which either the $^{9}Be(p,p_0)^{9}Be$ backscattering or the $^{9}Be(p,d_0)^{8}Be$ nuclear reaction peaks did not overlap with other signals. Energies in keV.

Table 2 – Differential cross-section σ, uncertainty Δσ and smoothed differential cross-section σ_{sm} for $^{9}Be(p,p_0)^{9}Be$ backscattering at a laboratory scattering angle of 165° in the energy range 400-4150 keV. The grey area from 2450-2950 keV indicates the incident proton energy range, where the data is the sum of the $^{9}Be(p,p_0)^{9}Be$ backscattering and the $^{9}Be(p,d_0)^{8}Be$ nuclear reaction cross-sections.

Table 3 – Differential cross-section σ and uncertainty Δσ of the $^{9}Be(p,d_0)^{8}Be$ nuclear reaction at a laboratory reaction angle of 165° in the energy range 400-4150 keV

Table 4 – Differential cross-section σ and uncertainty Δσ of the $^{9}Be(p,\alpha_0)^{6}Li$ nuclear reaction at a laboratory reaction angle of 165° in the energy range 400-1300 keV

Figure 1 – Typical EBS spectra for 2200 keV incident protons onto the multilayered targets with different Al thicknesses; a - 3.3×10^{18} at/cm², b - 27×10^{18} at/cm², c - 58×10^{18} at/cm². Incident angle is 0°, scattering angle is 165°.

Figure 2 – Energies of backscattered particles and nuclear reaction products vs. incident particle energy in the energy range 400-4150 keV: black solid lines – $^{9}Be(p,p_0)^{9}Be$, red dashed lines – $^{9}Be(p,d_0)^{8}Be$, blue dotted lines – $^{9}Be(p,\alpha_0)^{6}Li$ and magneta dash-dotted lines – $^{9}Be(p,\alpha_i)^{6}Li$ reactions at 165°. The vertical range indicates incident proton energies with an overlap between $^{9}Be(p,p_0)^{9}Be$ backscattering and the $^{9}Be(p,d_0)^{8}Be$ nuclear reaction

Figure 3 - Typical EBS spectrum for 1300 keV incident protons onto the multilayered target with 3.3×10^{18} at/cm² Al thickness. Incident angle is 0°, scattering angle is 165°.

Figure 4 – EBS spectrum for 2100 keV incident protons onto a bulk beryllium sample. Data points are experimental data, the dashed line is the extrapolated alpha signal, the solid line is the sum of a modeled spectrum made using cross-section data from this work plus the extrapolated alpha signal from the $^{8}Be\rightarrow2\times^{4}He$ fission reaction and the $^{9}Be+p\rightarrow\alpha_0+^{6}Li$ nuclear reaction. Vertical lines indicate the fitting range.

Figure 5 – Differential cross-section for $^{9}Be(p,p_0)^{9}Be$ backscattering at a laboratory scattering angle of 165° in the energy range 400-4150 keV. Black squares – this work, red circles – Liu for 170°, blue triangles – Mashkarov for 160.9°, green upside-down triangles – Tsan for 158.7°, dark yellow rhombs – Allab for 158.3°, magenta stars – Yasue for 150°, grey line – smoothed cross-section from this work.

Figure 6 – Differential cross-section for the $^{9}Be(p,d_0)^{8}Be$ nuclear reaction at a laboratory reaction angle of 165° in the energy range 400-4150 keV. Black squares – this work, red circles – Bertrand for 159.8°, blue triangles – Thomas for 138°, dark yellow upside-down triangles – Weber for 135°.

Figure 7 – Differential cross-section for the $^{9}Be(p,\alpha_0)^{6}Li$ nuclear reaction at a laboratory reaction angle of 165° in the energy range 400-1300 keV. Black squares – this work, red circles – Bertrand for 159.8°, blue triangles – Thomas for 138°.

Figure 8 – EBS spectra for 1.1, 1.3, 1.5, 1.7, 1.9, 2.3, 2.5, 2.7, 2.9, 3.1, 3.3, 3.5, 3.7, 4.1 MeV incident protons onto a bulk beryllium sample. Data points are experimental data, solid lines are simulations using the cross-section data from this work, dashed lines are simulated $^{9}Be(p,p_0)^{9}Be$ backscattering spectra, dotted lines are simulated $^{9}Be(p,d_0)^{8}Be$ nuclear reaction spectra, dash-dotted lines are simulated $^{9}Be(p,\alpha_0)^{6}Li$ nuclear reaction spectra., short dashed lines are simulations using smoothed $^{9}Be(p,p_0)^{9}Be$ cross-section

Table 1

Reaction\ Sample	Sample 1	Sample 2	Sample 3
9Be(p,p)9Be	–	1.75-2.5	2.7-3.7
9Be(p,d)8Be	0.4-0.7; 1.3-1.7	2.05-2.45	3.05-3.3

Table 2

E_p (keV)	σ (mb/sr)	Δσ (mb/sr)	σ_{sm} (mb/sr)
490	157	7	
591	109	5	
692	85	4	
792	58	3	
812	53	3	
833	49	3	
853	39	3	
873	32	2	
893	26.1	2.0	
913	21.0	1.8	
933	18.4	1.6	
953	23.5	1.9	
973	52.3	2.9	
993	100	5	
1013	144	6	
1033	162	7	
1054	145	7	
1074	124	6	
1094	129	6	
1114	121	6	
1134	116	5	
1154	106	5	
1174	101	4	
1194	102	5	
1244	102	5	
1294	116	5	
1345	129	6	
1395	127	6	
1445	115	5	
1495	105	5	
1545	101	5	
1595	94	5	
1645	87	4	
1746	75	3	
1796	73	3	
1846	74	3	
1896	71	3	
1946	73	3	
1996	75	3	
2046	75	3	
2096	80	4	
2146	80	4	
2196	85	4	
2246	84	4	
2296	87	4	
2346	90	4	
2397	103	5	

2447	122	5	
2497	180	8	
2547	203	9	
2597	119	6	
2647	83	4	
2697	67	4	
2747	57	3	
2797	53	3	53
2847	45.8	2.6	46.6
2897	45.5	2.9	42.0
2947	36.8	2.3	38.9
2997	34.7	2.2	36.9
3047	37.6	2.4	35.9
3097	35.1	2.4	35.1
3147	36.4	1.9	34.6
3197	35.1	1.8	35.4
3247	33.9	1.7	35.3
3297	34.4	1.7	34.7
3347	35.9	1.9	34.7
3397	35.6	1.8	34.3
3447	32.9	1.7	34.3
3497	33.9	1.8	34.1
3547	34.6	1.8	34.4
3597	33.6	1.7	34.9
3647	35.9	1.9	35.5
3698	35.5	1.9	36.2
3748	39.5	2.1	36.5
3798	36.8	2.0	36.5
3848	35.2	1.9	36.9
3898	36.9	2.0	37.1
3948	36.9	2.0	37.5
3998	37.3	2.0	37.9
4048	40.6	2.7	38.6
4098	39.5	2.7	39.4
4148	39.7	2.6	40.4

Table 3

E_p (keV)	σ (mb/sr)	Δσ (mb/sr)
389	24.3	1.2
490	19.0	0.9
591	12.9	0.6
692	6.6	0.3
953	7.2	0.5
973	4.3	0.3
993	2.1	0.23
1294	16.8	0.8
1345	26.2	1.2
1395	26.3	1.2
1445	23.8	1.1
1545	27.1	1.3
1595	29.0	1.3
1645	28.1	1.3
1695	28.7	1.4
1746	33.2	1.9
1796	19.0	1.3
2046	15.6	0.8
2096	15.8	0.8
2146	13.6	0.8
2196	12.5	0.9
2246	10.1	0.8
2296	8.8	0.8
2346	6.1	0.7
2397	4.4	0.6
2447	2.8	0.26
2947	5.0	1.1
2997	5.5	1.3
3047	6.5	1.2
3097	4.5	0.7
3147	5.1	0.8
3197	5.3	0.7
3247	6.4	1.0
3297	7.6	1.7
3347	10.0	1.7
3397	10.7	1.5
3447	8.4	1.5
3497	7.8	1.4
3547	8.0	1.6
3597	9.5	1.6
3647	10.9	2.1
3698	11.0	1.6
3748	11.3	1.8
3798	11.2	1.6
3848	8.7	1.7
3898	12.1	1.9
3948	9.7	1.3

3998	11.5	1.4
4048	11.3	1.3
4098	10.6	1.5
4148	13.2	1.5

Table 4

E_p (keV)	σ (mb/sr)	Δσ (mb/sr)
389	23.1	1.1
490	7.8	0.4
591	8.1	0.4
692	8.8	0.4
792	9.8	0.5
812	10.3	0.5
833	11.1	0.5
853	11.3	0.5
873	11.3	0.5
893	12.4	0.6
913	12.6	0.6
933	13.0	0.6
953	12.1	0.6
973	9.5	0.4
993	8.1	0.4
1013	7.1	0.3
1033	6.8	0.3
1054	6.9	0.3
1074	6.9	0.3
1094	7.5	0.4
1114	7.6	0.4
1134	7.7	0.4
1154	8.3	0.4
1174	8.3	0.4
1194	8.9	0.4
1244	10.6	0.5
1294	10.0	0.5

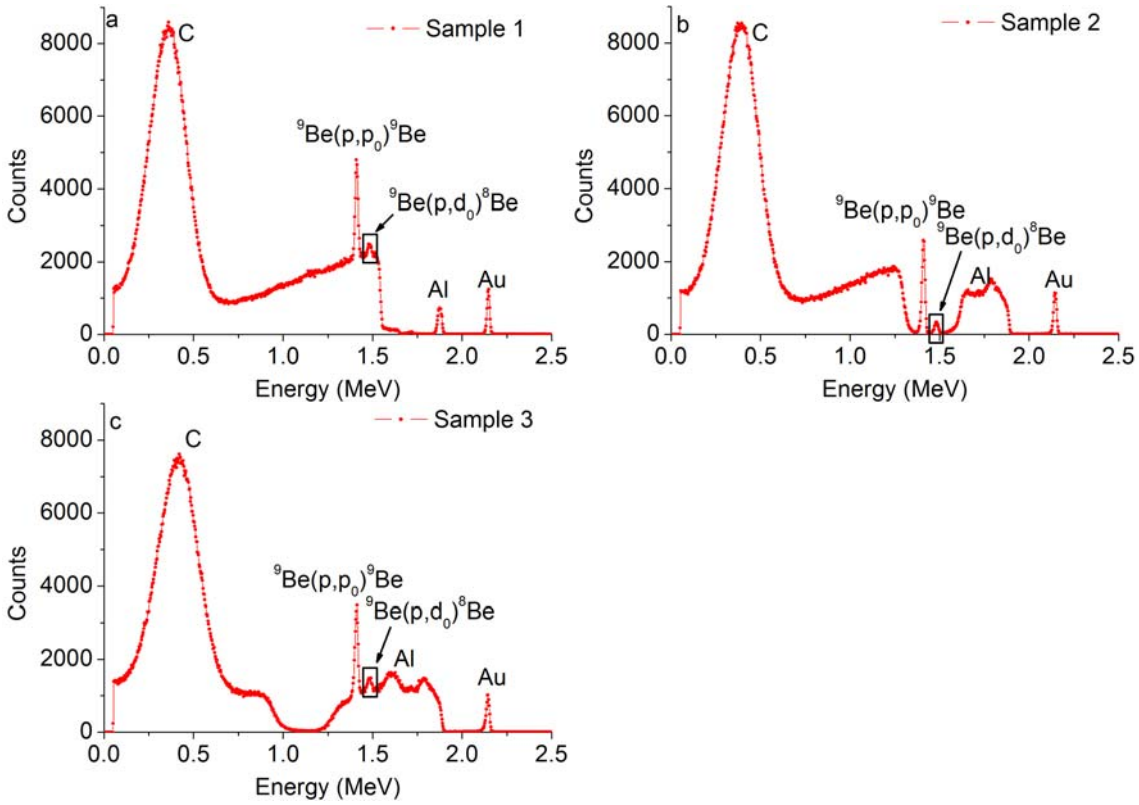
a
Sample 1
C
^{9}Be(p,p$_0$)^{9}Be
^{9}Be(p,d$_0$)^{8}Be
Al
Au
Counts
Energy (MeV)
b
Sample 2
C
^{9}Be(p,p$_0$)^{9}Be
^{9}Be(p,d$_0$)^{8}Be
Al
Au
Counts
Energy (MeV)
c
Sample 3
C
^{9}Be(p,p$_0$)^{9}Be
^{9}Be(p,d$_0$)^{8}Be
Al
Au
Counts
Energy (MeV)

Figure 1

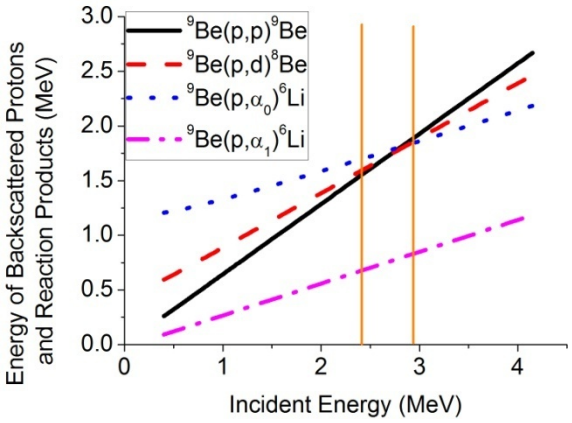
Energy of Backscattered Protons and Reaction Products (MeV)
Incident Energy (MeV)
$^{9}Be(p,p)^{9}Be$
$^{9}Be(p,d)^{8}Be$
$^{9}Be(p,\alpha_0)^{6}Li$
$^{9}Be(p,\alpha_1)^{6}Li$
0.0
0.5
1.0
1.5
2.0
2.5
3.0
0
1
2
3
4

Figure 2

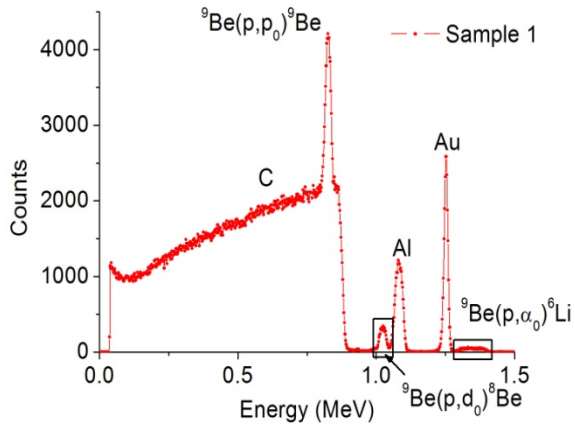
^{9}Be(p,p$_0$)^{9}Be
Sample 1
Counts
4000
3000
2000
1000
0
C
Au
Al
^{9}Be(p,α$_0$)^{6}Li
0.0
0.5
1.0
1.5
Energy (MeV)
^{9}Be(p,d$_0$)^{8}Be

Figure 3

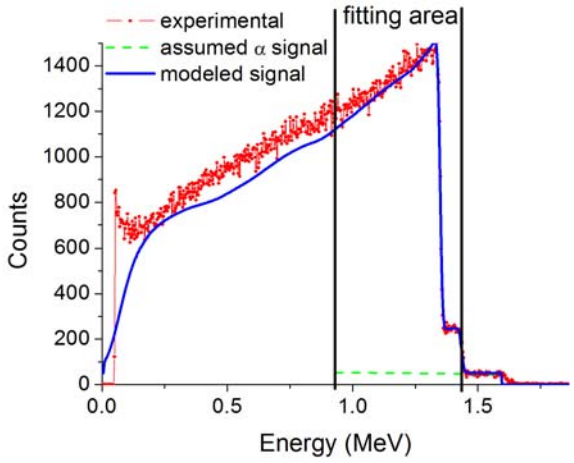
experimental
assumed α signal
modeled signal
fitting area
Counts
Energy (MeV)
0
200
400
600
800
1000
1200
1400
0.0
0.5
1.0
1.5

Figure 4.

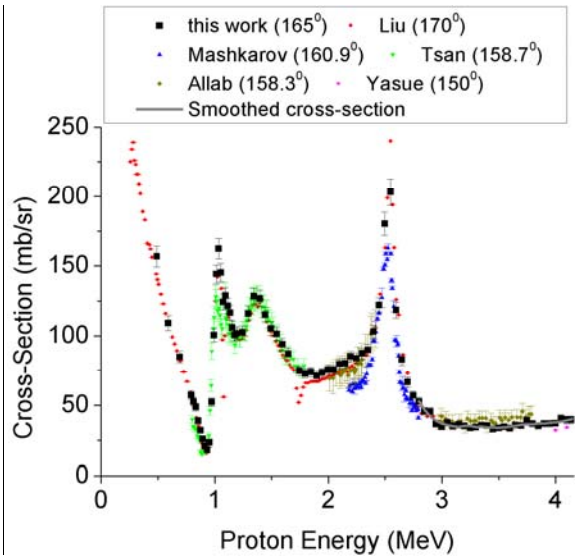
this work (165°)
Liu (170°)
Mashkarov (160.9°)
Tsan (158.7°)
Allab (158.3°)
Yasue (150°)
Smoothed cross-section
Cross-Section (mb/sr)
Proton Energy (MeV)
0
50
100
150
200
250
0
1
2
3
4

Figure 5.

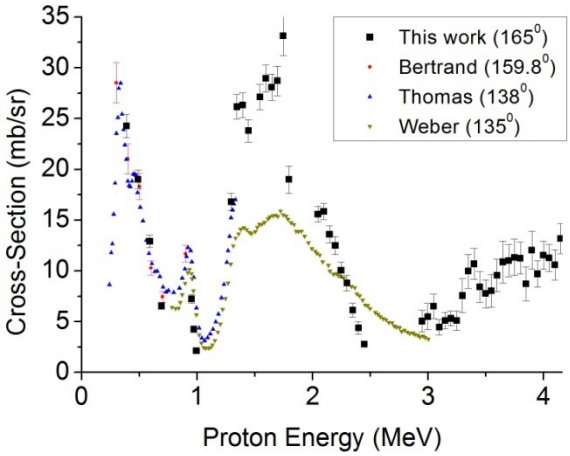
This work (165^0)
Bertrand (159.8^0)
Thomas (138^0)
Weber (135^0)
Cross-Section (mb/sr)
Proton Energy (MeV)
0
5
10
15
20
25
30
35
0
1
2
3
4

Figure 6

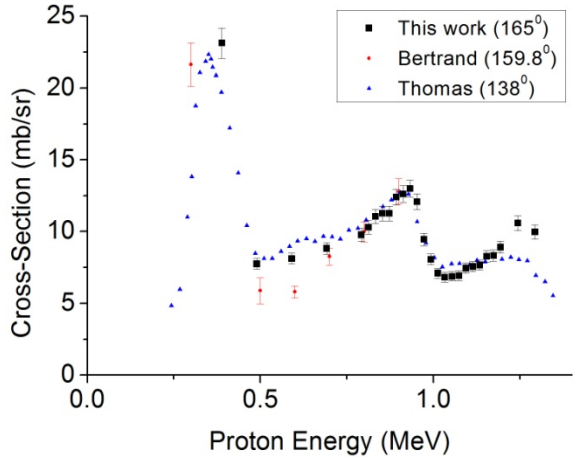
This work (165^0)
Bertrand (159.8^0)
Thomas (138^0)
Cross-Section (mb/sr)
Proton Energy (MeV)
0
5
10
15
20
25
0.0
0.5
1.0

Figure 7

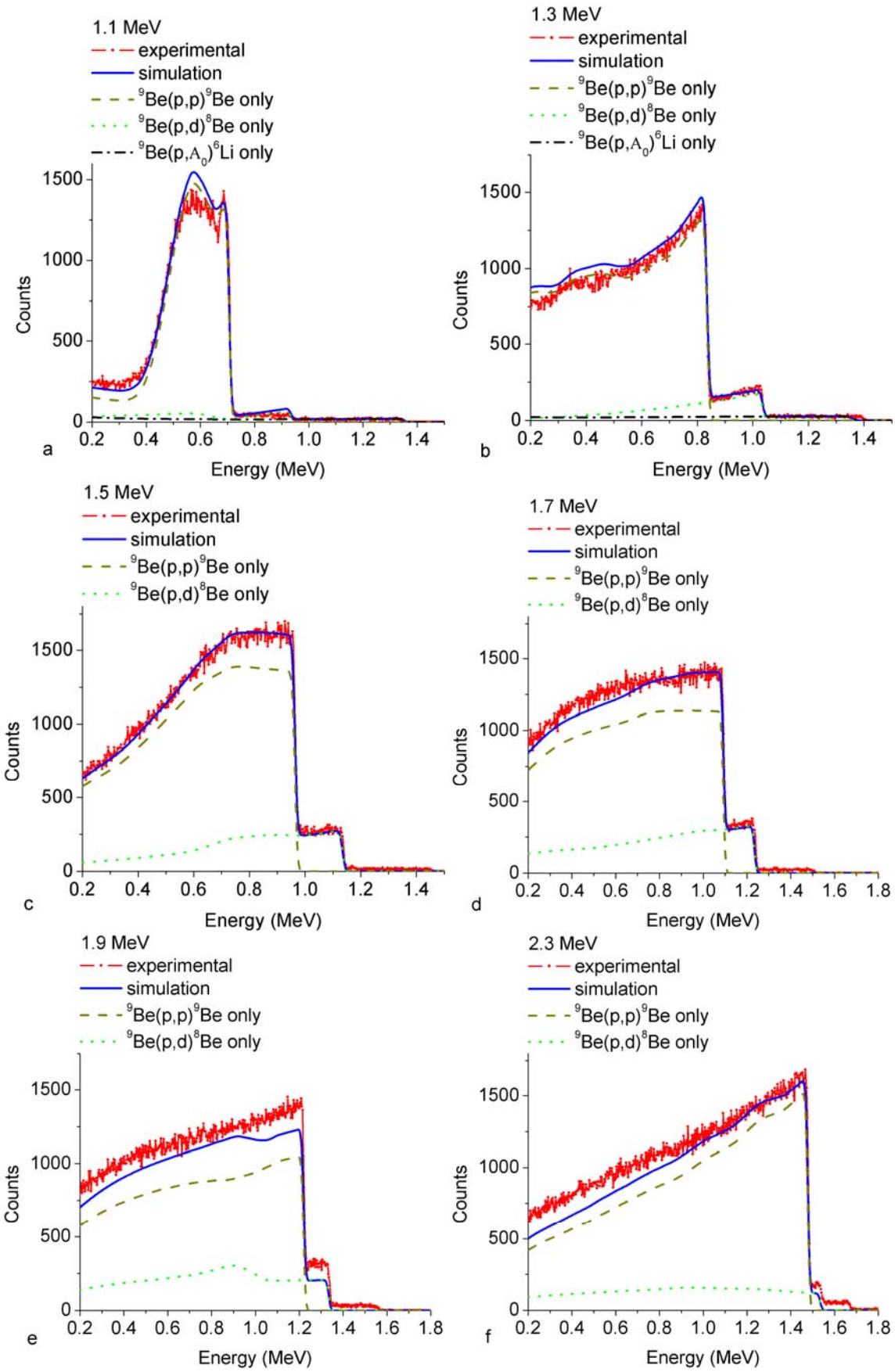
1.1 MeV
experimental
simulation
^{9}Be(p,p)^{9}Be only
^{9}Be(p,d)^{8}Be only
^{9}Be(p,A_0)^{6}Li only
Counts
Energy (MeV)
a
1.3 MeV
experimental
simulation
^{9}Be(p,p)^{9}Be only
^{9}Be(p,d)^{8}Be only
^{9}Be(p,A_0)^{6}Li only
Counts
Energy (MeV)
b
1.5 MeV
experimental
simulation
^{9}Be(p,p)^{9}Be only
^{9}Be(p,d)^{8}Be only
Counts
Energy (MeV)
c
1.7 MeV
experimental
simulation
^{9}Be(p,p)^{9}Be only
^{9}Be(p,d)^{8}Be only
Counts
Energy (MeV)
d
1.9 MeV
experimental
simulation
^{9}Be(p,p)^{9}Be only
^{9}Be(p,d)^{8}Be only
Counts
Energy (MeV)
e
2.3 MeV
experimental
simulation
^{9}Be(p,p)^{9}Be only
^{9}Be(p,d)^{8}Be only
Counts
Energy (MeV)
f

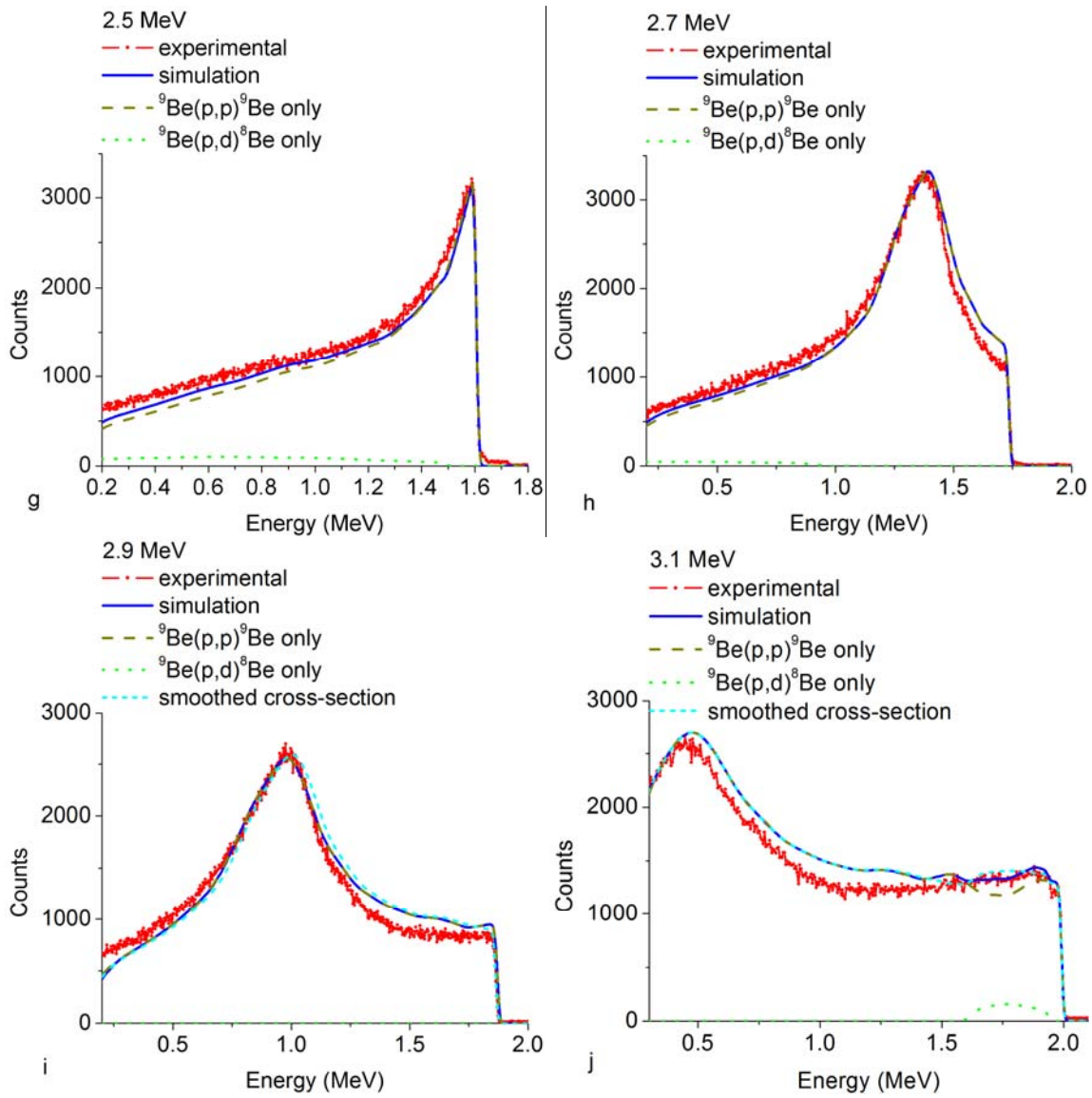
2.5 MeV
experimental
simulation
^{9}Be(p,p)^{9}Be only
^{9}Be(p,d)^{8}Be only
Counts
Energy (MeV)
g
2.7 MeV
experimental
simulation
^{9}Be(p,p)^{9}Be only
^{9}Be(p,d)^{8}Be only
Counts
Energy (MeV)
h
2.9 MeV
experimental
simulation
^{9}Be(p,p)^{9}Be only
^{9}Be(p,d)^{8}Be only
smoothed cross-section
Counts
Energy (MeV)
i
3.1 MeV
experimental
simulation
^{9}Be(p,p)^{9}Be only
^{9}Be(p,d)^{8}Be only
smoothed cross-section
Counts
Energy (MeV)
j

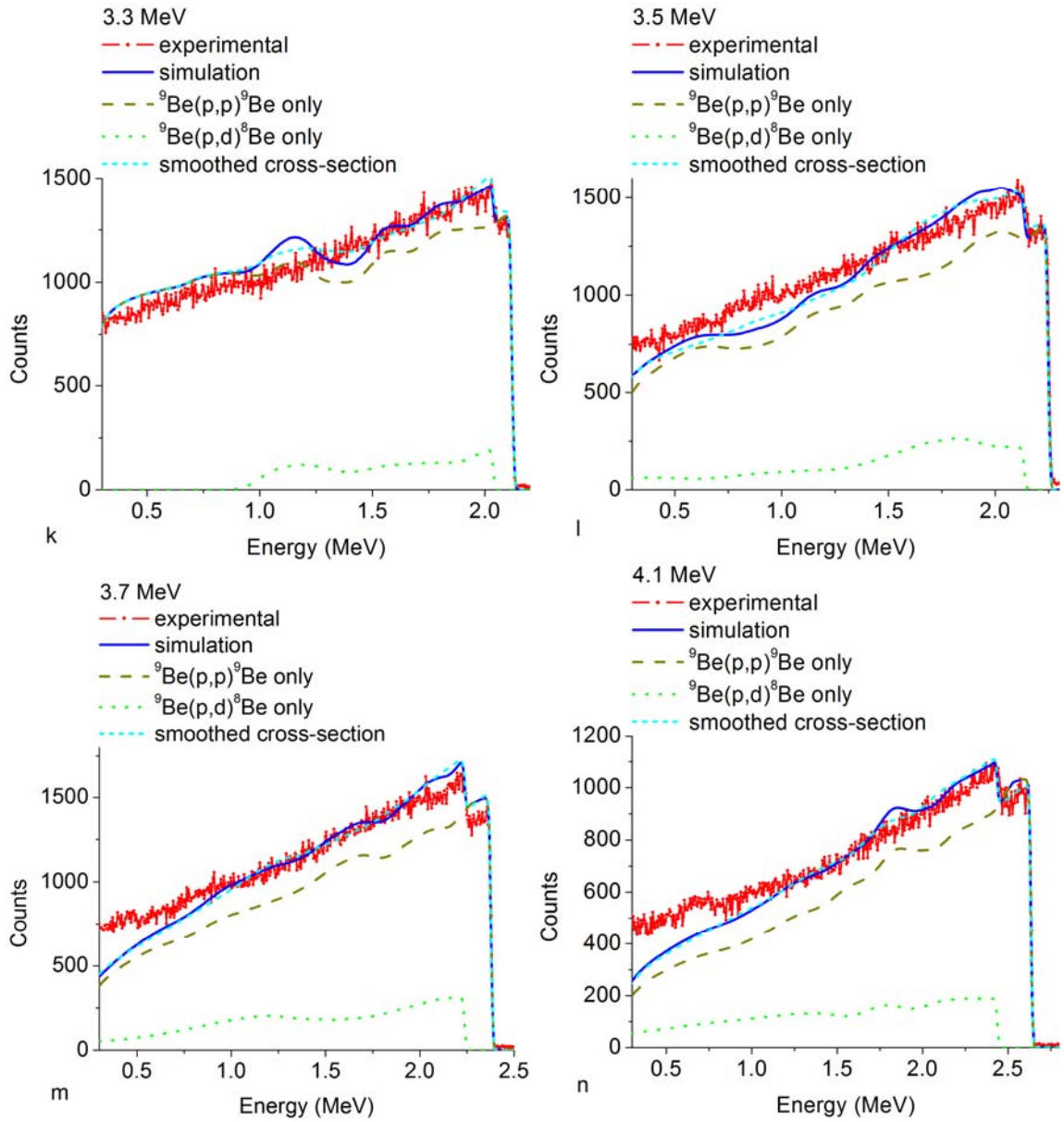
3.3 MeV
experimental
simulation
^{9}Be(p,p)^{9}Be only
^{9}Be(p,d)^{8}Be only
smoothed cross-section
Counts
Energy (MeV)
k
3.5 MeV
experimental
simulation
^{9}Be(p,p)^{9}Be only
^{9}Be(p,d)^{8}Be only
smoothed cross-section
Counts
Energy (MeV)
l
3.7 MeV
experimental
simulation
^{9}Be(p,p)^{9}Be only
^{9}Be(p,d)^{8}Be only
smoothed cross-section
Counts
Energy (MeV)
m
4.1 MeV
experimental
simulation
^{9}Be(p,p)^{9}Be only
^{9}Be(p,d)^{8}Be only
smoothed cross-section
Counts
Energy (MeV)
n

Figure 8